

Topological defects in confined populations of spindle-shaped cells

Guillaume Duclos, Christoph Erlenkämper, Jean-François Joanny and Pascal Silberzan*

Most spindle-shaped cells (including smooth muscles and sarcomas) organize *in vivo* into well-aligned 'nematic' domains^{1–3}, creating intrinsic topological defects that may be used to probe the behaviour of these active nematic systems. Active non-cellular nematics have been shown to be dominated by activity, yielding complex chaotic flows^{4,5}. However, the regime in which live spindle-shaped cells operate, and the importance of cell-substrate friction in particular, remains largely unexplored. Using *in vitro* experiments, we show that these active cellular nematics operate in a regime in which activity is effectively damped by friction, and that the interaction between defects is controlled by the system's elastic nematic energy. Due to the activity of the cells, these defects behave as self-propelled particles and pairwise annihilate until all displacements freeze as cell crowding increases^{6,7}. When confined in mesoscopic circular domains, the system evolves towards two identical $+1/2$ disclinations facing each other. The most likely reduced positions of these defects are independent of the size of the disk, the cells' activity or even the cell type, but are well described by equilibrium liquid crystal theory. These cell-based systems thus operate in a regime more stable than other active nematics, which may be necessary for their biological function.

Ever since Otto Lehman⁸ and Georges Friedel⁹ showed that the microscopic structure of nematic or smectic phases could be inferred from a careful observation of their characteristic structural defects, the study of liquid crystals has gone hand in hand with a characterization of the topological defects—that is, singular points in the orientation field—that affect the long-range orientational order¹⁰.

Far-from-equilibrium active nematics are no exception to that rule. These systems are composed of interacting elongated self-propelled particles that actively align with their neighbours, in a nematic or polar phase¹¹. These collective behaviours are observed in a wide variety of systems and length scales, and share common universal properties¹¹. For example, actin microfilaments or microtubules associated with their molecular motors^{4,5,12,13}, elongated motile cells^{1,3,14} or bacteria¹⁵, or more macroscopic systems, such as fish swimming in schools¹⁶, exhibit strong long-range alignment.

Spindle-shaped cells spontaneously form nematic arrangements *in vivo* in diverse situations, such as smooth muscles or pathological tissues such as sarcomas. It has been shown^{1–3} that, when plated on a surface at sufficiently high density, these cells self-align in a bidimensional nematic phase. As time proceeds, the cell density increases via cell proliferation, which increases the nematic ordering but also gradually freezes the cell movements^{6,17–20}, resulting in a juxtaposition of large, perfectly ordered domains whose directors

are not aligned. These domains are separated by topological defects trapped in the structure³.

On the theoretical side, several recent works have addressed the behaviours of defects in active nematics by adding active terms to the hydrodynamic equations of liquid crystals. Although there are differences between these approaches²¹, they all converge in showing that active systems differ from passive nematics by the spontaneous motion of the $+1/2$ topological defects, which behave as self-propelled particles^{22,23}, the creation/annihilation of pairs of defects of opposite signs^{22–24}, or the associated velocity correlations in the bulk^{25,26}. Most of the active systems that have been identified so far operate in a regime where activity is large and viscous damping dominates cell-substrate friction⁴. However, live cells are known to develop adhesion with their substrate, yielding a large friction²¹. Here, by studying the topological defects in a nematic cell monolayer, we propose to assess the contribution of friction in these systems.

We first present experimental results dealing with proliferating spindle-shaped NIH 3T3 mouse embryo fibroblasts that interact via steric hindrance when plated on fibronectin-coated glass substrates (Supplementary Methods). Retinal pigment epithelial (RPE1) cells and C2C12 mouse myoblasts behaved very similarly. To study the structural defects in this system, we dynamically mapped the orientation field and the velocity field after confluence, defined as the point where the surface is entirely covered by cells (Fig. 1a–c). The root-mean-square (r.m.s.) velocity, taken as an indirect measurement of the cells' activity²⁵ (Supplementary Fig. 1), decreased over time and reached very low values associated with local rearrangements (Fig. 1d). The velocity correlation length increased from 50 μm to 300 μm (the latter corresponding to about 20 cell sizes) in typically two days¹⁹, as the system evolved from an isotropic to a nematic state (Fig. 1d, insets).

At high cell density, the fusion of the well-oriented domains was hindered by topological defects characteristic of nematic phases (Figs 1b and 2a). According to the usual classification¹⁰, these disclinations were either of topological charge $s = +1/2$ or $s = -1/2$ (Fig. 2a).

With time, the number of defects decreased because of pairwise annihilation, as described below (Fig. 2b and Supplementary Fig. 2). The density of defects then stabilized after typically 40 h, as the proliferation-induced increase in cell density caused the displacements of the cells to gradually freeze. This final steady state corresponded to a distance between defects of typically 650 μm (Fig. 2b).

Investigating the individual dynamics of these defects, we observed that $-1/2$ defects did not move significantly, as expected from symmetry arguments. In contrast, $+1/2$ defects were animated

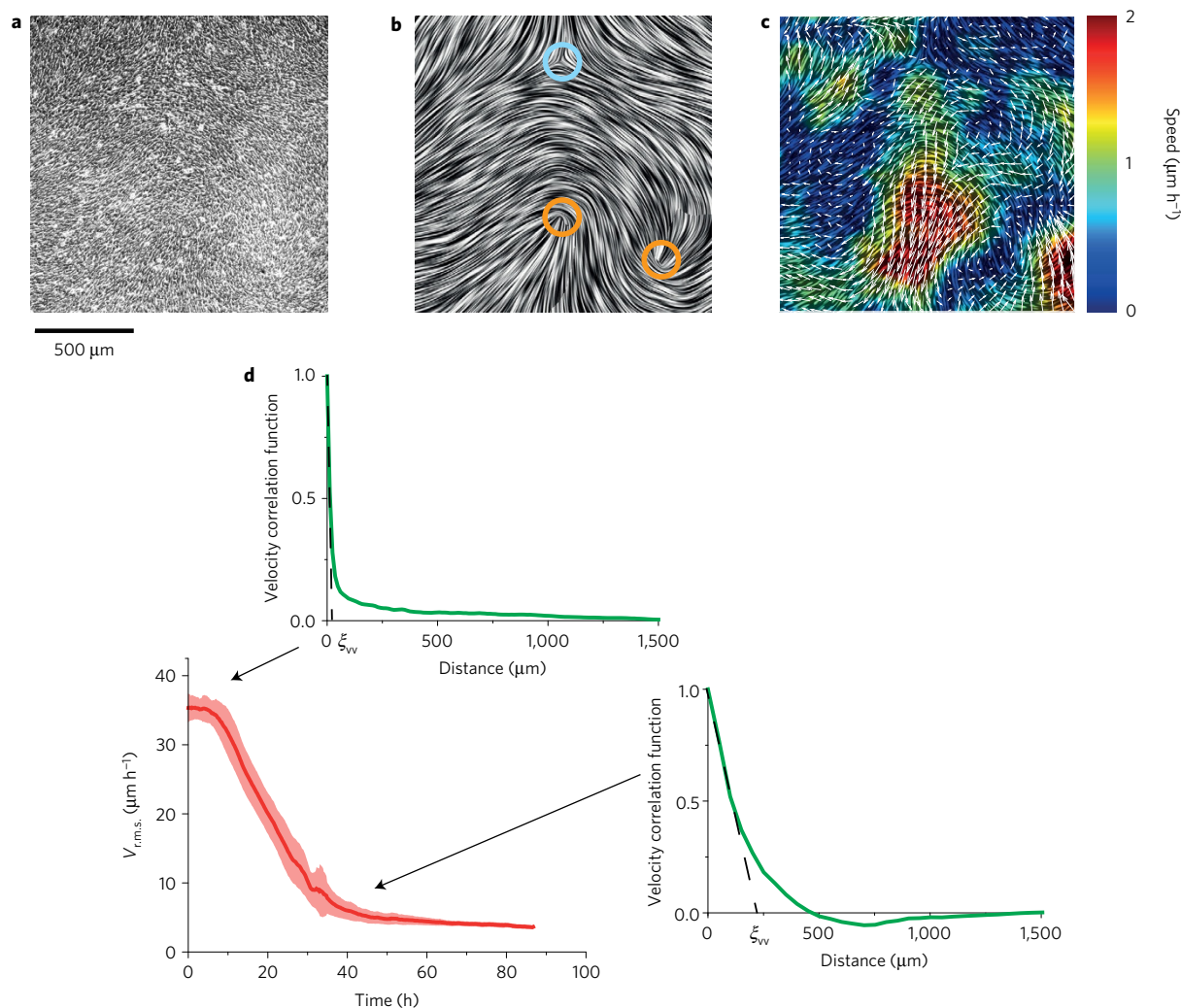


Figure 1 | Orientation field in a NIH 3T3 monolayer. **a**, Phase contrast image 40 h post-confluence. **b**, Line integral convolution (LIC) representation showing the field lines of the orientation field. Defects are outlined with coloured circles ($-1/2 = \text{cyan}$, $+1/2 = \text{orange}$). **c**, Complex velocity flows developing in the monolayer in the vicinity of the $+1/2$ defects. **d**, The r.m.s. velocity decreases with time until reaching very low values (red curve, coloured area is the standard deviation, $N=17$). At the same time, the velocity correlation length ξ_{vv} increases (green curves).

by a directed motion with their ‘comet tail’ forward (Fig. 2c), which is the signature of an active contractile system^{23,24}. In contractile systems, pairs of defects can in principle be created via a splay instability^{25,27}. However, in practice, we did not observe the creation of defects in our experiments; their high number at confluence resulted from local ordering at the isotropic–nematic transition^{1,28}. This observation suggests that the system is dominated by a large cell–substrate friction²¹, which is consistent with our estimate of the hydrodynamic screening length of approximately one cell size (Supplementary Note 1).

This active migration of the $+1/2$ defects was accompanied by large-scale collective displacements around the defect itself in the monolayer (Fig. 1c). Since the system is dominated by friction, these flows are attributed to the gradients of active stress. The situation is therefore different from other active nematic systems characterized by a high activity and a low friction, and resulting in more unstable systems exhibiting complex chaotic flows and the creation of many defects^{4,5}.

Very interestingly, the directed movement of the $+1/2$ defects took place along lines of ‘kinks’ that separated perfectly ordered domains (Supplementary Fig. 3). Similar lines have previously been observed in numerical simulations for nematics in a regime dominated by friction^{25,29}. The local order parameter

therefore mirrors an effective energy landscape where the lines of kinks correspond to valleys confining the migration of the disclinations.

The microscopic origin of the decrease in the number of defects could be traced to pairwise annihilations between defects of opposite topological charges (Supplementary Fig. 4A)¹⁰. When $+1/2$ and $-1/2$ defects came closer than typically $150\text{ }\mu\text{m}$, they moved towards each other with symmetrical trajectories until they merged and annihilated at time t_a . Their separation d close to their annihilation point was compatible with a law $d \propto \sqrt{t_a - t}$ (Supplementary Fig. 4B), as predicted in the case where activity is secondary to pairwise topological attraction^{22–24,30}. Of note, the ratio of the cell–substrate friction to the activity defines a time $\tau \sim 1 - 10\text{ h}$ (Supplementary Note 1) that compares well with the experimentally measured annihilation time of 4 h for defects initially separated by $150\text{ }\mu\text{m}$ (Supplementary Fig. 4B).

To model our system, we relied on liquid crystal theory. Dealing with a two-dimensional nematic system, and using the classical one-constant approximation, the Frank–Oseen elastic free energy \mathcal{F} reads:

$$\mathcal{F} = \frac{K}{2} \int_{\text{FOV}} |\nabla \mathbf{n}|^2 dx dy = \frac{K}{2} \int_{\text{FOV}} \left[\left(\frac{d\varphi}{dx} \right)^2 + \left(\frac{d\varphi}{dy} \right)^2 \right] dx dy \quad (1)$$

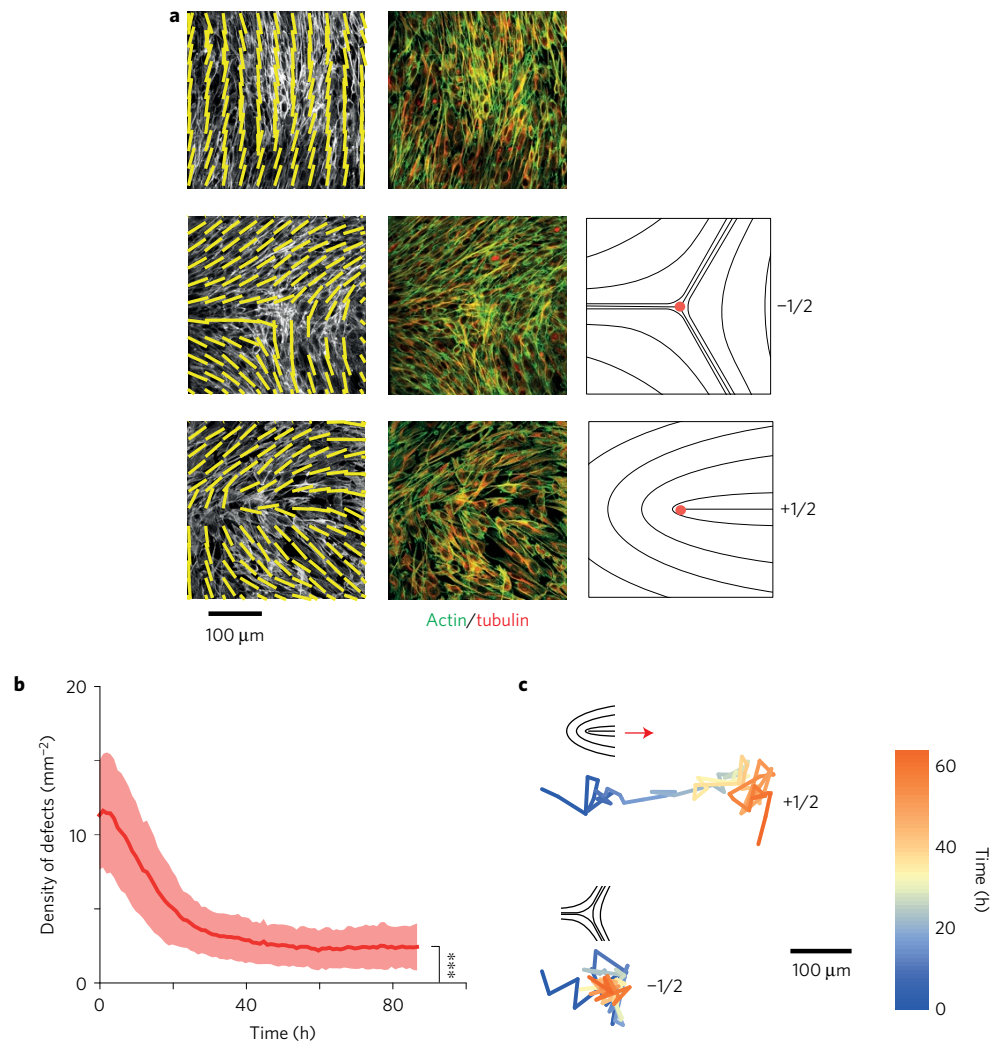


Figure 2 | Topological defects in a NIH 3T3 monolayer. **a**, Identification of the two types of defects that can be observed. Left: orientation field superimposed on actin fluorescence images. Centre: same area where actin and tubulin have been labelled. Right: schematics of the $+1/2$ and $-1/2$ defects. **b**, Time evolution of the number of defects in the monolayer. A finite density is reached at long times. Note that the small positive fluctuations are measurement artefacts: in our experiments, defects are not created. (Coloured area is the standard deviation, $N=137$ FOV from nine independent experiments.) **c**, $+1/2$ and $-1/2$ defects have very different dynamics. $+1/2$ defects have a clear directed motion whereas $-1/2$ defects diffuse about their initial position.

where FOV is the field of view, \mathbf{n} is the local director, K is the Frank constant and φ is the polar angle¹⁰.

The elastic energy decreased over time as the tissue reshaped itself during its development and the cells' activity decreased (Supplementary Fig. 5). The positions of the defects correlated well with the local maxima of the free energy (Supplementary Fig. 5).

For a better control of the defect localization and the associated cellular collective motion, we confined the cells in micropatterned adhesive disks of various radii, R_0 , ranging from 250 μm to 400 μm. As previously noted, edge cells aligned with the boundary of the domains, which mathematically fixed the total charge of the nematic tissue to $+1$. In two dimensions, however, the stable configuration consists in two defects of charge $+1/2$ (ref. 10) when the domain's radius is smaller than the orientation correlation length (typically 500 μm; ref. 3).

Similarly to the boundary-free situation, several randomly distributed defects were initially present in each domain when the cells reached confluence. As the density increased, the defects pairwise annihilated until two facing $+1/2$ defects remained (Figs 3a–d and 4a,b and Supplementary Fig. 6 and Supplementary Movie 1), as predicted. Their most likely radial position, r , then

scaled with the domain's radius: $r = \alpha R_0$ with $\alpha = 0.67 \pm 0.02$ (Standard Error) (Fig. 4d,e). These radial positions were pairwise-uncorrelated (Pearson coefficient <0.2 for all disks' radii). Remarkably, the same experiments performed in the presence of blebbistatin, which affects myosin contractility and therefore the activity of the cells (and possibly their Frank constant), or even with another cell line presenting similar nematic alignment (C2C12 myoblasts), gave the exact same result qualitatively and quantitatively (Fig. 4d and Supplementary Fig. 7). Therefore, the position of the defects appears to be a robust characteristic of the nematic order adopted by spindle-shaped cells. Finally, the two defects positioned themselves preferentially along a diameter, as expected from symmetry arguments (Fig. 4a,b,f).

To understand this behaviour, we minimized the Frank–Oseen free energy (equation (1)) with imposed circular boundary conditions and a perfect alignment with the boundary³¹ (Supplementary Note 2). The position of the two defects then resulted from a balance between the alignment of the cells at the boundary and the repulsion between these two defects of identical charge.

We determined the nematic orientation field under these conditions and the corresponding energy of the system for

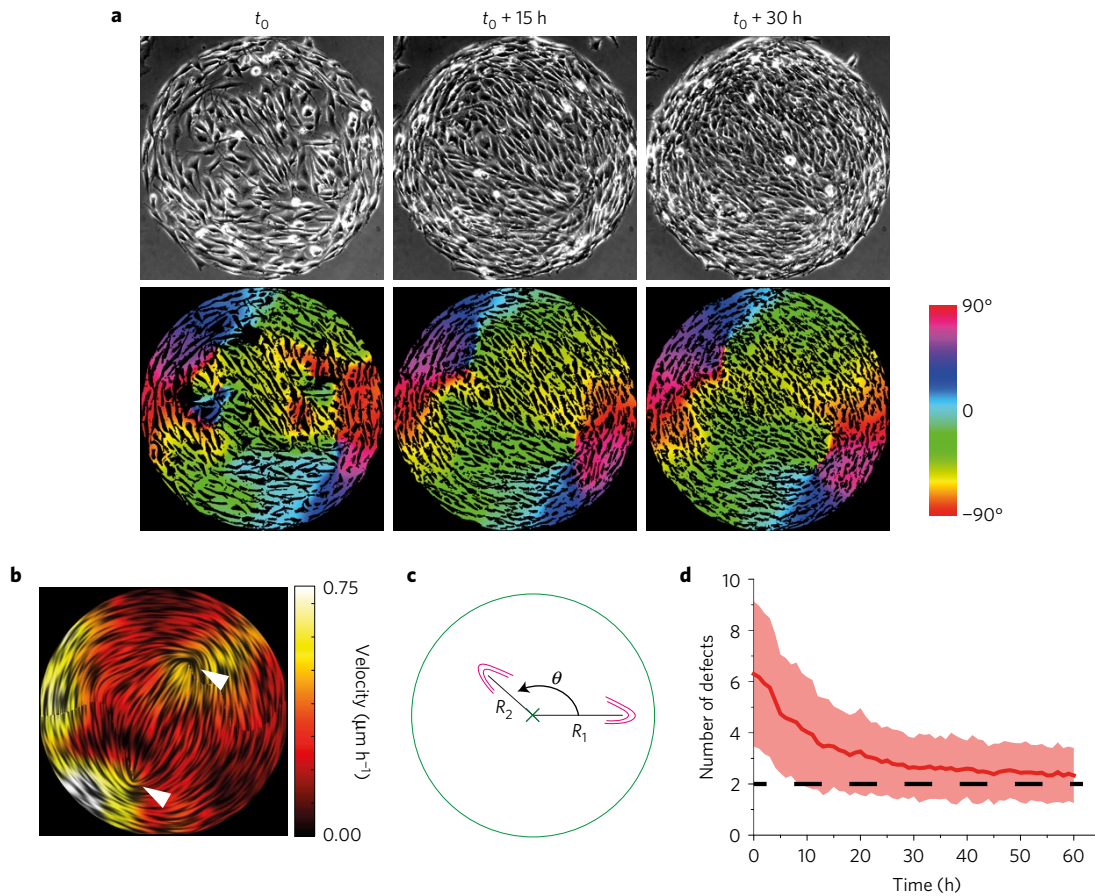


Figure 3 | Effect of confinement in a disk. a, With time, the number of defects decreases and they reach a stable position. **b**, Identification of the two $+1/2$ defects in the LIC representation (white triangles). **c**, Schematic of the defect positions and convention. There is a unique way to position the two defects in the disk with one defect on the horizontal axis and $[R_1 > 0, R_2 > 0, 0 < \theta < \pi]$. **d**, At long times, there remain only two defects in the disk. (Coloured area is the standard deviation, $N_{\text{disks}} = 150$.) All panels: NIH 3T3 cells, $R_0 = 350 \mu\text{m}$.

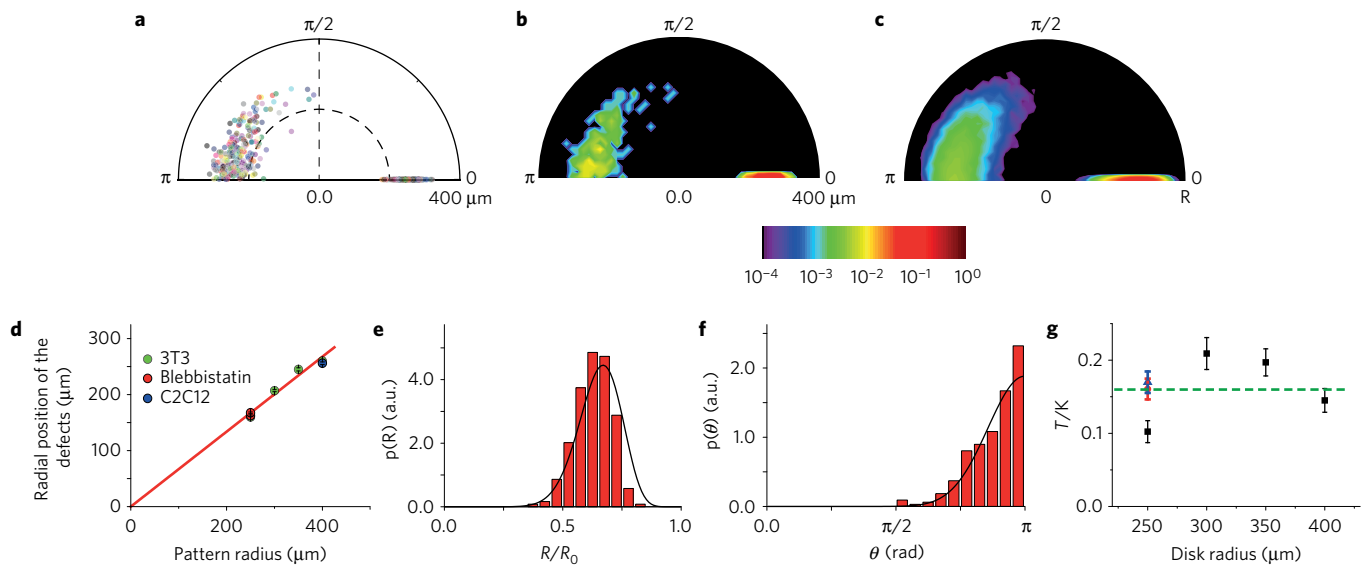


Figure 4 | Defects' positions in the disks. a, Point representation of the defects. Each point corresponds to a defect and each colour to a different domain ($N_{\text{disks}} = 486$). NIH 3T3 cells, $R_0 = 400 \mu\text{m}$. **b**, Same as **a**, where the colour code gives the probability density of defects. **c**, Simulation of the probability density of defects with $T/K = 0.2$ ($N_{\text{defects}} = 20,000$). **d**, The radial defects' position r scales with the radius of the pattern R_0 . Green points: NIH 3T3 cells. The red line is a linear fit: $r = 0.67R_0$. Note that this positioning is independent of activity (red points are in the presence of blebbistatin) or even cell type (blue points: C2C12 cells). Error bars are standard error of the mean. **e, f**, Distributions of the positions of the defects along R (**e**) and θ (**f**). The outcome of the nematic disk model is superimposed (black line). $R_0 = 400 \mu\text{m}$, NIH 3T3 cells, $N = 486$. **g**, The effective temperature (in units of K) in various conditions remains much smaller than 1, demonstrating the small contribution of activity in these systems. Error bars are standard errors, $N > 276$ disks for each point.

defects at polar positions $(r, 0)$ and (r, ϑ) (Fig. 3c). The system minimizes its energy for $\vartheta = \pi$ and $r = 5^{-1/4}R_0 \sim 0.668R_0$ (see Supplementary Note 2 and Fig. 4c). This solution is in excellent agreement with the experimental results (Supplementary Fig. 8). Importantly, this most likely position of the defects is predicted to be independent of both the activity and the Frank elastic constant, explaining why the same position was experimentally observed for different cell types and in the presence of myosin inhibitor (Supplementary Fig. 7). Of note, taking into account the finite size of the defects does not significantly affect these conclusions (Supplementary Note 2).

Cells being active particles, the positions of the two defects are described by distributions about their most likely positions (Fig. 4a,b,e,f). Computing the energy landscape allowed the definition of an effective temperature T corresponding to the widths of these distributions (Supplementary Fig. 9 and Supplementary Note 2). Fitting model to data in each experimental condition, we consistently measured small temperatures in units of K : $0.1 < T/K < 0.2$, independently of the size of the domain (Fig. 4g). K being the only energy scale in this system, this result confirms that, at high cell density, the activity of these cellular nematics, although at the origin of the self-induced motion of the $+1/2$ defects, is effectively damped by cell–substrate friction. The interaction between defects in nematic cell layers is thus controlled by the elastic nematic energy.

We have shown that spindle-shaped cells self-assemble as active nematics. Upon confinement, the distribution of the positions of the topological defects is extremely robust with respect to the size of the confinement, activity or even cell type. The description of our results by a simple nematic disk model confirms that activity is effectively damped by cell–substrate friction, and their robustness suggests that this conclusion might be generalized to other biological tissues composed of spindle-shaped cells. These observations show that these cell monolayers operate in a regime more stable and less chaotic than other active nematics. The extrapolation of these results should shed new light on the behaviour and dynamics of spindle-shaped tissues, including sarcoma.

Methods

Methods, including statements of data availability and any associated accession codes and references, are available in the [online version of this paper](#).

Received 24 March 2016; accepted 3 August 2016;
published online 12 September 2016

References

1. Elsdale, T. Parallel orientation of fibroblasts *in vitro*. *Exp. Cell Res.* **51**, 439–450 (1968).
2. Kemkemer, R., Kling, D., Kaufmann, D. & Gruler, H. Elastic properties of nematoid arrangements formed by amoeboid cells. *Eur. Phys. J. E* **1**, 215–225 (2000).
3. Duclos, G., Garcia, S., Yevick, H. G. & Silberzan, P. Perfect nematic order in confined monolayers of spindle-shaped cells. *Soft Matter* **10**, 2346–2353 (2014).
4. Sanchez, T., Chen, D. T. N., DeCamp, S. J., Heymann, M. & Dogic, Z. Spontaneous motion in hierarchically assembled active matter. *Nature* **491**, 431–434 (2012).
5. Keber, F. C. *et al.* Topology and dynamics of active nematic vesicles. *Science* **345**, 1135–1139 (2014).
6. Angelini, T. E. *et al.* Glass-like dynamics of collective cell migration. *Proc. Natl Acad. Sci. USA* **108**, 4714–4719 (2011).
7. Puliafito, A. *et al.* Collective and single cell behavior in epithelial contact inhibition. *Proc. Natl Acad. Sci. USA* **109**, 739–744 (2012).
8. Lehman, O. *Flüssige Kristalle* (Engelmann, 1904).

9. Friedel, G. Les états mésomorphes de la matière. *Ann. Phys. Paris* **18**, 273–474 (1922).
10. de Gennes, P.-G. & Prost, J. *The Physics of Liquid Crystals* 2nd edn (Oxford Univ. Press, 2003).
11. Marchetti, M. C. *et al.* Hydrodynamics of soft active matter. *Rev. Mod. Phys.* **85**, 1143–1189 (2013).
12. Schaller, V. & Bausch, A. R. Topological defects and density fluctuations in collectively moving systems. *Proc. Natl Acad. Sci. USA* **110**, 4488–4493 (2013).
13. DeCamp, S. J., Redner, G. S., Baskaran, A., Hagan, M. F. & Dogic, Z. Orientational order of motile defects in active nematics. *Nat. Mater.* **14**, 1110–1115 (2015).
14. Kemkemer, R., Teichgräber, V., Schrank-Kaufmann, S., Kaufmann, D. & Gruler, H. Nematic order-disorder state transition in a liquid crystal analogue formed by oriented and migrating amoeboid cells. *Eur. Phys. J. E* **110**, 101–110 (2000).
15. Wensink, H. H. *et al.* Meso-scale turbulence in living fluids. *Proc. Natl Acad. Sci. USA* **109**, 14308–14313 (2012).
16. Vicsek, T. & Zafeiris, A. Collective motion. *Phys. Rep.* **517**, 71–140 (2012).
17. Nnetu, K. D., Knorr, M., Käs, J. A. & Zink, M. The impact of jamming on boundaries of collectively moving weak-interacting cells. *New J. Phys.* **14**, 115012 (2012).
18. Park, J.-A. *et al.* Unjamming and cell shape in the asthmatic airway epithelium. *Nat. Mater.* **14**, 1040–1048 (2015).
19. Garcia, S. *et al.* Physics of active jamming during collective cellular motion in a monolayer. *Proc. Natl Acad. Sci. USA* **112**, 15314–15319 (2015).
20. Bi, D., Yang, X., Marchetti, M. C. & Manning, M. L. Motility-driven glass and jamming transitions in biological tissues. *Phys. Rev. X* **6**, 021011 (2016).
21. Doostmohammadi, A., Adamer, M. F., Thampi, S. P. & Yeomans, J. M. Stabilization of active matter by flow-vortex lattices and defect ordering. *Nat. Commun.* **7**, 10557 (2016).
22. Giomi, L., Bowick, M. J., Mishra, P., Sknepnek, R. & Cristina Marchetti, M. Defect dynamics in active nematics. *Phil. Trans. R. Soc. A* **372**, 20130365 (2014).
23. Pismen, L. M. Dynamics of defects in an active nematic layer. *Phys. Rev. E* **88**, 050502 (2013).
24. Giomi, L., Bowick, M. J., Ma, X. & Marchetti, M. C. Defect annihilation and proliferation in active nematics. *Phys. Rev. Lett.* **110**, 228101 (2013).
25. Thampi, S. P., Golestanian, R. & Yeomans, J. M. Velocity correlations in an active nematic. *Phys. Rev. Lett.* **111**, 118101 (2013).
26. Doostmohammadi, A. *et al.* Cell division: a source of active stress in cellular monolayers. *Soft Matter* **11**, 7328–7336 (2015).
27. Giomi, L. Geometry and topology of turbulence in active nematics. *Phys. Rev. X* **5**, 1–11 (2015).
28. Elsdale, T. & Wasoff, F. Fibroblast cultures and dermatoglyphics: the topology of two planar patterns. *Wilhelm Roux Arch. Dev. Biol.* **180**, 121–147 (1976).
29. Thampi, S. P., Golestanian, R. & Yeomans, J. M. Active nematic materials with substrate friction. *Phys. Rev. E* **90**, 062307 (2014).
30. Tóth, G., Denniston, C. & Yeomans, J. M. Hydrodynamics of topological defects in nematic liquid crystals. *Phys. Rev. Lett.* **88**, 105504 (2002).
31. Galanis, J., Nossal, R., Losert, W. & Harries, D. Nematic order in small systems: measuring the elastic and wall-anchoring constants in vibrofluidized granular rods. *Phys. Rev. Lett.* **105**, 168001 (2010).

Acknowledgements

We thank I. Bonnet, A. Buguin, J. Prost, L. Vallon, H. Yevick and the members of the ‘Biology-Inspired Physics at Mesoscales’ (BIPM) group for discussions. The BIPM group and the ‘Physical Approaches of Biological Problems’ group are members of the CeTisPhyBio Labex. The BIPM group is a member of the Institut Pierre-Gilles de Gennes pour la Microfluidique.

Author contributions

G.D. and P.S. designed the research. G.D. performed the experiments and C.E. developed the theory. P.S. and J.-F.J. supervised the research. All authors analysed the data and participated in writing the manuscript.

Additional information

Supplementary information is available in the [online version of the paper](#). Reprints and permissions information is available online at www.nature.com/reprints. Correspondence and requests for materials should be addressed to P.S.

Competing financial interests

The authors declare no competing financial interests.

Methods

Cell culture. NIH 3T3 fibroblasts (kind gift from K. Laud-Duval, Institut Curie), C2C12 myoblasts (kind gift from C. Théry, Institut Curie) and RPE1 (kind gift from M. Dahan, Institut Curie) cells were cultured in Dulbecco's modified Eagle's medium (High glucose + GlutaMAX, Gibco) supplemented with 10% fetal bovine serum (FBS, Sigma) and 1% antibiotics solution [penicillin (10,000 units ml⁻¹) + streptomycin (10 mg ml⁻¹); Gibco] at 37 °C, 5% CO₂ and 90% humidity. Cells were initially plated at low density on a microscope glass slide. When indicated, fibronectin (Invitrogen) was used at a concentration of 10 µg ml⁻¹ to coat the glass surface. Blebbistatin (Sigma) was used at concentrations of 1 µM and 3 µM that significantly affected the activity (Supplementary Fig. 7). Low-calcium medium (Calcium-free DMEM, FBS 10%, Penstrep 1%, 50 µM Calcium) was used to stop cell division. The cells were initially cultured in regular medium and then re-plated with low-calcium medium. All cell lines were tested mycoplasma-free.

Time-lapse microscopy. Time-lapse multifield experiments were performed in phase contrast on an automated inverted microscope (Olympus IX71) with ×10 objectives and equipped with both thermal and CO₂ regulation. Typical field of view (FOV) was 1.5 mm × 1.5 mm. The displacements of the sample and the acquisitions with a charge-coupled device (CCD) camera (Retiga 4000R, QImaging) were controlled through Metamorph (Universal Imaging) software. The typical delay between two successive images of the same field was set to 10 min. High-resolution fluorescence images on fixed cells were acquired with an inverted spinning disk confocal microscope (Nikon) with a ×40 oil immersion objective. Cells were fixed in 4% paraformaldehyde (PFA), permeabilized in 0.1% Triton X-100 and blocked in 10% FBS in phosphate buffered saline (PBS) solution. Actin was labelled using Alexa 546 phalloidin (Life Technologies, 1:500). Alpha-Tubulin was labelled using anti-alpha Tubulin Alexa Fluor 488 (eBioscience, 1:1,000). Hoechst 33342 (Sigma, 1:10,000) was used to mark the nuclei.

Image processing. Most of the image processing was performed using the ImageJ public domain software³². The orientation field was obtained by computing the local structure tensor with ImageJ's plugin OrientationJ³³. For representation purposes, we used a Line integral convolution (LIC)³⁴ under Matlab.

The local order parameter Q_{loc} map was obtained by computing the order parameter over square sub-windows Ω of size 8 µm:

$$Q_{\text{loc}} = \sqrt{\langle \cos 2\theta \rangle_{(x,y) \in \Omega}^2 + \langle \sin 2\theta \rangle_{(x,y) \in \Omega}^2}. \quad Q_{\text{loc}} \text{ varies between 0 and 1.}$$

Q_{loc} was used to detect and track the defects after thresholding. The map of the order parameter (Supplementary Note 2) was determined from immunofluorescence images on actin after fixation.

The velocity field in the monolayer was mapped by particle image velocimetry (PIV) analysis³⁵. Stacks of images were analysed with a custom-made PIV

algorithm based on the MatPIV software package for MatLab (MathWorks). The time between successive analysed images was 60 min. The window size was set to 128 pixels = 95 µm with a 0.5 overlap. The normalized velocity correlation function was classically defined as $\langle (\mathbf{V}(\mathbf{R}) \cdot \mathbf{V}(\mathbf{0}) / |\mathbf{V}(\mathbf{0})|^2) \rangle$.

Micropatterning technique. Clean glass substrates were first uniformly coated with a protein-repellent layer (interpenetrated gel of acrylamide and polyethylene glycol)^{36,37}. A photoresist mask was then deposited on top of the layer by classical photolithography methods and air plasma was used to locally etch the protein-repellent coating through this mask. Substrates were incubated in fibronectin (10 µg ml⁻¹) after which the photoresist was removed yielding a cell repellent substrate where fibronectin domains have been defined.

Statistical analysis. Statistical analysis was performed with Matlab (Mathworks) or Origin (Originlab). Experiments were performed in at least three replicas, with more than 130 disks and up to 430 disks per condition. Unless stated otherwise, distributions were compared using a two-sample *t*-test. Error bars represent the SDs over all the FOVs or disks analysed (pooling all experiments in a single set).

The most likely radial position of the defects was initially obtained by fitting a bi-Gaussian function to the distribution.

Modelling of the nematic disk and minimization of the Frank–Oseen free energy in disks was performed with Matlab (MathWorks, v. R2014b).

Data availability. The data that support the plots within this paper and other findings of this study are available from the corresponding author upon request.

References

32. Rasband, W. S. *ImageJ v1.46b* (US National Institutes of Health, 1997–2012).
33. Rezakhaniha, R. *et al.* Experimental investigation of collagen waviness and orientation in the arterial adventitia using confocal laser scanning microscopy. *Biomech. Model. Mechanobiol.* **11**, 461–473 (2012).
34. Cabral, B. & Leedom, L. C. Imaging vector fields using line integral convolution. *Proc. 20th Annu. Conf. Comput. Graph. Interact. Tech. - SIGGRAPH'93* 263–270 (ACM Press, 1993).
35. Deforet, M. *et al.* Automated velocity mapping of migrating cell populations (AVeMap). *Nat. Methods* **9**, 1081–1083 (2012).
36. Tourovskaia, A., Figueroa-Masot, X. & Folch, A. Long-term microfluidic cultures of myotube microarrays for high-throughput focal stimulation. *Nat. Protoc.* **1**, 1092–1104 (2006).
37. Deforet, M., Hakim, V., Yevick, H. G., Duclos, G. & Silberzan, P. Emergence of collective modes and tri-dimensional structures from epithelial confinement. *Nat. Commun.* **5**, 3747 (2014).